Received: 28 May 2022 | Revised: 17 July 2022 | Accepted: 18 July 2022

DOI: 10.1002/eom2.12266

RESEARCH ARTICLE

EcoMat FUNCTIONAL MATERIALS FOR GREEN ENERGY AND ENVIRONMENT WILEY

Elucidation and modulation of active sites in holey graphene electrocatalysts for H_2O_2 production

Ki Hwan Koh[1,2] | **Amir Hassan Bagherzadeh Mostaghimi**[3] | **Qiaowan Chang**[1,4] | **Yu Joong Kim**[2] | **Samira Siahrostami**[3] | **Tae Hee Han**[2] | **Zheng Chen**[1,4]

[1]Department of Nano Engineering, University of California San Diego, San Diego, California, USA

[2]Department of Organic and Nano Engineering, Human-Tech Convergence Program, Hanyang University, Seoul, Republic of Korea

[3]Department of Chemistry, University of Calgary, Calgary, Alberta, Canada

[4]Program of Chemical Engineering, Sustainable Power & Energy Center (SPEC), University of California San Diego, San Diego, California, USA

Correspondence
Samira Siahrostami, Department of Chemistry, University of Calgary, 2500 University Drive NW, Calgary, Alberta, Canada.
Email: samira.siahrostami@ucalgary.ca

Tae Hee Han, Department of Organic and Nano Engineering, Human-Tech Convergence Program Hanyang University Seoul 04763, Republic of Korea.
Email: than@hanyang.ac.kr

Zheng Chen, Department of Nano Engineering, University of California San Diego, La Jolla, CA 92093, USA.
Email: zhengchen@eng.ucsd.edu

Funding information
American Chemical Society Petroleum Research Fund, Grant/Award Number: 59989-DNI5; University of Calgary's Canada First Research Excellence Fund Program; National Research Foundation of Korea, Grant/Award Number: 2020R1A2C2101652; Jacob School of Engineering at UC San Diego

Abstract

Selective electrochemical oxygen reduction (ORR) toward a two-electron ($2e^-$) pathway is an eco-friendly alternative method for H_2O_2 synthesis to replace the energy-intensive anthraquinone oxidation process. Carbon-based electrocatalysts (CBEs) show great potential for practical H_2O_2 synthesis. However, their complex structures make it challenging to determine the nature of active sites and to precisely control them. Herein, we show that precise modulation of the chemistry and structures of holey graphene with edge sites enriched by oxygen-containing functional groups can facilitate $2e^-$ ORR. These combined functionalities could improve ORR performance under various pH conditions, for example, resulting in an average of 95% H_2O_2 selectivity, ~97% Faraday efficiency, high productivity of 2360 mol kg_{cat}^{-1} h^{-1} in alkaline media. Density functional theory calculations on the oxygen functional groups at the edge sites revealed the most active site for $2e^-$ ORR is a synergy between ether (C—O—C) and carbonyl (C═O) functional groups with nearly zero overpotential.

KEYWORDS

electrocatalyst, graphene, hydrogen peroxide, oxygen reduction reaction

1 | INTRODUCTION

Hydrogen peroxide (H_2O_2) is an important chemical with a wide range of applications, including chemical synthesis, disinfection, wastewater treatment, and industrial bleaching.[1,2] The general industrial process for H_2O_2 production (so-called anthraquinone oxidation) has several drawbacks, including poor energy efficiency and the need for organic waste disposal. Thus, alternative approaches for sustainable and efficient H_2O_2 generation have attracted considerable attention.[3] Electrochemical H_2O_2 synthesis through the two-electron ($2e^-$) oxygen reduction reaction (ORR) shows significant advantages over other processes because it can leverage renewable energy

sources and allows for on-site direct production of H_2O_2.[4–6] In principle, ORR proceeds through two competitive pathways of $2e^-$ or $4e^-$, with H_2O_2 and H_2O as the end products, respectively. The formation of HOO* intermediate and its further protonation or dissociation, are the primary determinant of selective ORR toward $2e^-$ or $4e^-$ pathways, respectively.[4,5] Based on this mechanistic understanding, a rational structure design of the electrocatalysts is necessary for high activity and selectivity.[7–10] Numerous studies have focused on the development of electrocatalysts with tunable structures, such as noble metals[11–16] and alloys,[17–19] transition metal-based catalysts,[20–22] single-atom induced catalysts[23–28] and carbon-based materials.[29–35] Precious metals and their mercury alloys have the highest activity and selectivity for $2e^-$ ORR, but their high cost and the hazardous properties of mercury hinders their widespread application.[35,36] In comparison, carbon-based electrocatalysts (CBEs) have been attracting attention as efficient, sustainable, and cost-effective alternatives.

To enhance the electrocatalytic performance of CBEs, the electronic structures are often modulated by introducing various types of defects. In particular, previous studies indicate that heteroatom doping,[29,31,33,37,38] intrinsic defects,[30] and oxygen functionalization[34,35] are effective strategies for defect engineering in promoting the $2e^-$ ORR. However, the nature of the active sites in lattice defects remains unclear due to the inherent complexity of the disordered structures of CBEs. Most CBEs have intrinsic defects, such as Stone-Wales defects and innumerable types of vacancies forming defect clusters.[39] As these structural defects alter the local electronic structure or charge density of the electron system for sp^2-bonding, CBEs become active for overall ORR of $2e^-$ or $4e^-$ pathway.[40] Several studies reported that diverse intrinsic defects have been identified with superior active sites in a $4e^-$ ORR through facilitating the adsorption of oxygen and lowering the energy barrier for the following reactions toward H_2O.[41–43] In contrast, Bao and coworkers demonstrated that a wide variety of intrinsic defect configurations induce favorable $2e^-$ ORR toward H_2O_2 generation.[30] Although proper design of the defect structures, in line with these reports, is necessary to achieve the desired reaction, practical challenges remain for precisely controlling the lattice defects and crystalline structure, which is a major hindrance to further improving activity and selectivity for selective $2e^-$ ORR.

Herein, we report a tactical approach for atomic scale structural engineering using functionalized holey graphene to facilitate highly efficient H_2O_2 production via $2e^-$ ORR. The designed graphene is made by "punching" process followed by oxidation. Specifically, the disordered regions in the hexagonal crystalline network of graphene are removed, leaving holes on the basal plane by simple heat treatment in air. The nanohole inevitably includes the high density of the edge site,[44] which is further modified with specific oxygen functional groups to achieve better activity and selectivity. Such a tactical approach leads to oxidized-holey graphene (O-HGr) that has a high density of edge active sites with ether (C—O—C) and carbonyl (C═O) functional groups. In addition, the holey structure can also significantly improve mass transfer in the stacked graphene layers in the catalytic electrodes, which is confirmed by systematic electrochemical impedance spectroscopy (EIS) measurement. This specially designed electrocatalyst shows high $2e^-$ ORR selectivity of average 95% in a wide potential range (0.2 to 0.8 V, all the following potential values are referred to RHE unless specified) and high productivity (2360 mol kg_{cat}^{-1} h^{-1}, ~97% of Faradaic efficiency [FE]) with excellent long-term stability. Density functional theory (DFT) calculations are performed to investigate the activity trends across a range of possible oxygen functional groups at oxygen-enriched holes. This analysis reveals the nature of active site that originates from a synergy between ether (C—O—C) and carbonyl (C═O) functional groups with minimum $2e^-$ ORR overpotential. It also reveals that the activity drops in acidic and neutral media originate from protonation of C═O functional groups to form C—OH.

2 | RESULTS AND DISCUSSION

Among various nanostructure carbon materials, graphene oxide (GO) is an attractive precursor for defect engineering because it has a large proportion of sp^3 hybridizations derived from abundant oxygen functionalities to sp^2 carbon atoms. Although several studies have aimed to control the intrinsic defects of graphene electrocatalysts, we took a different approach to conduct defect engineering. In our synthesis, the defect clusters on the basal plane of the graphene (Gr) were removed, leaving the nano-hole behind. This holey graphene (HGr) was then functionalized with specific oxygen functional groups to form O-HGr. The detailed synthesis process is illustrated in Figure 1. A mild thermal reduction of GO at 500°C in argon allowed formation of abundant defective spots on the basal plane of Gr. HGr was subsequently obtained by a simple "punching" process where Gr was heated in air at 410 °C. Because in the basal plane of Gr, the disordered areas are much combustible due to their poor thermal stability compared with well-ordered areas, they react with oxygen first and burn to form CO_2, leaving holes on the surface of Gr. The reaction temperature was determined by the thermogravimetric analysis (TGA) result (Figure S1). For the oxidation process, previous studies have shown various types of approaches including acid treatment,[45] electrochemical oxidation,[46] and O_2 etching.[47] As each method resulted in the different

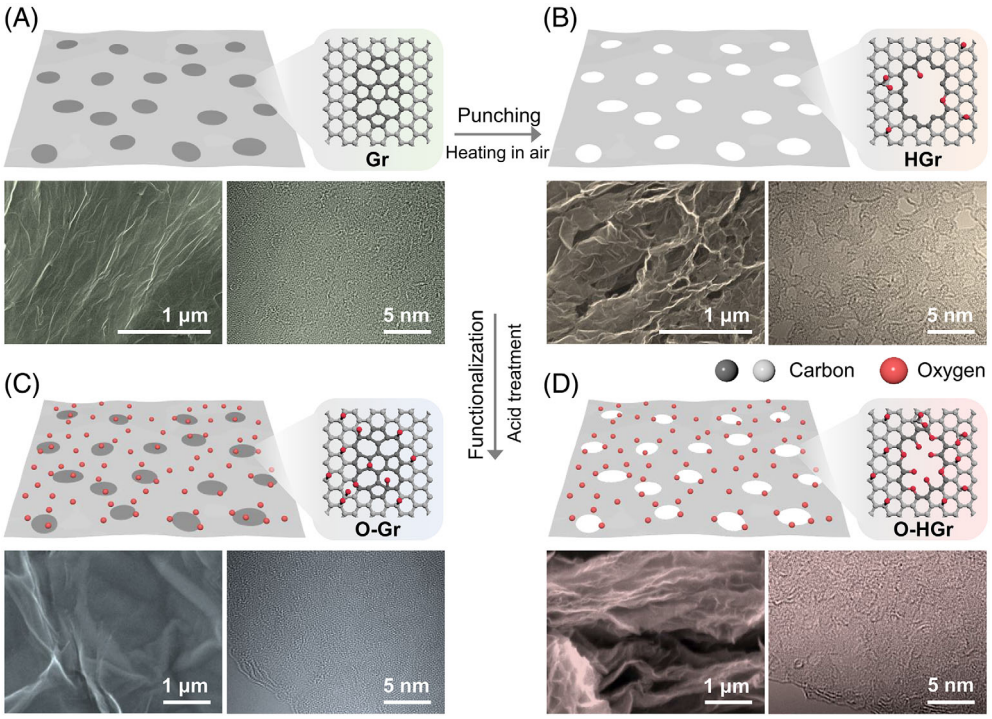

FIGURE 1 Schematic illustration of the synthesis process and microscopic characterization of graphene electrocatalysts. SEM (left) and TEM (right) images of (A), Gr (B) HGr, (C) O-Gr, and (D) O-HGr

surface chemistries, we selected the nitric acid (HNO_3) treatment to introduce the specific oxygen functional groups. It has been well known that since broken bonds at the edges develop radical groups with accessible and highly active electrons, carbon atoms localized on graphene edges are more vulnerable to the chemical reaction than those on the crystalline basal plane.[48] Besides, the reaction mechanism on the edges differs from that of the basal plane. Thus, we can expect that HGr should exhibit distinct oxidation behavior from Gr with more selective functional groups at the edges of holes. Both graphenes of HGr and Gr were finally oxidized into O-HGr and O-Gr by reflux in the acid.

Scanning electron microscopic (SEM) and transmission electron microscopic (TEM) images in Figure 1 and Figure S2 show a clear change in the microscopic morphologies of the Gr before and after the punching. SEM images (Figure 1A and C) for the non-holey Gr and O-Gr exhibited a typical appearance of graphene-based materials, showing two-dimensional (2D) flat sheets with fine wrinkles. On the nanometer scale, common disordered structures were observed in TEM images. In the case of HGr and O-HGr, not only macro-porous structures but meso- and micro-porous sheets were observed in SEM and TEM images, respectively. These distinctive porous features are beneficial to enhancing the mass transport of oxygen during the reaction. A distribution histogram of hole diameter was determined by counting 400 holes from the representative TEM images (Figure S3). Furthermore, these kinds of 2D graphene morphologies have been proved to have fundamental importance in various electrocatalysis fields,[49] especially in $2e^-$ ORR in recent years.[50] The crystalline and defective structures were further visualized by XRD and Raman spectra (Figure S4). A typical XRD pattern of Gr showed a broad peak at 2θ value of 25.2°, which corresponds to the (002) plane of the graphitic structure.[51] When the disordered area in the basal plane of Gr was removed, the peak became much sharper and shifted to a higher 2θ value of 26.2°, which indicates a decreased interlayer distance from 0.36 nm to 0.34 nm. A possible explanation to account for this physical variation is that since the crystallographic defects in Gr generate lattice distortion which, in turn, causes crystal expansion in the c-axis lattice parameter,[51] the absence of the lattice defects in HGr leads to the decrease in interlayer distance. Furthermore, displacement of carbon atoms from the well-ordered crystalline structures should be a leading cause for broadening of the (002) Bragg peak, which is a possible contribution to the sharper (002) peak of HGr than that of Gr. The introduction of oxygen functional groups on the graphene surface made the (002) peak broader, and *d*-spacing increased again to 0.37 nm for O-Gr and O-HGr. Defective characteristics were investigated by comparing intensity ratio of D and G bands (I_D/I_G) in the Raman spectra. The I_D/I_G value of 0.80 for Gr increased to 0.84 for HGr due to the formation of in-plane holes. After oxidation, the value of I_D/I_G of Gr further increased by 0.1 for O-Gr while a relatively small variation of 0.02 was observed for O-HGr, implying the different response of Gr and HGr upon oxidation.

Along with intrinsic defects, oxygen functional groups are another crucial factor in determining the ORR performance. Figure 2A shows the Fourier-transform infrared spectroscopy (FT-IR) spectra for all the samples. The representative spectrum of GO shows various oxygen species. The characteristic of random distribution of diverse C—O groups on GO is represented with a broad band at 900–1350 cm^{-1}. In this wide frequency range, hydroxyl, carboxyl and ether groups have contributions in the α (900–1100 cm^{-1}) and β (1100–1280 cm^{-1}) regions, while the γ (1280–1400 cm^{-1}) arises from the presence of epoxide groups.[52] Three other apparent peaks at 1640, 1750 and 3000–3700 cm^{-1} are attributed to the sp^2-hybridized C═C (in-plane vibrations), C═O double bond (carbonyl and carboxyl) and O-H (hydroxyl and carboxyl), respectively.[52] For the followed results of structure characterization, we use terms "C—O—C", "C═O" and "O═C—O" as symbols for ether, carbonyl and carboxyl groups, respectively. Most of the oxygen species disappeared after thermal reduction in the spectrum of Gr. Further heat treatment of Gr in air resulted in the reintroduction of C—O—C, O═C—O, and C═O groups into HGr, which were further confirmed by X-ray photoelectron spectroscopy (XPS) and electron energy loss spectroscopy (EELS) results. After oxidation, the spectra for O-Gr and O-HGr looked similar, with more distinct peaks of ether (C—O—C) and carbonyl (C═O).

Based on the FT-IR results, XPS was used to elucidate the chemical state of the oxygen functional groups, with the survey spectra, specific C 1 s spectra and deconvoluted O 1 s spectra shown in Figure S5–S7. The detailed information of the peak deconvolution is summarized in Table S2 and S3 (ESI†). The specific oxygen contents are presented in Figure 2B, which compares the specific contributions of various oxygen species. The quantified atomic concentrations (atomic %) of oxygen were calculated to be 10.30, 18.04, 39.10, and 31.26 for Gr, HGr, O-Gr, and O-HGr, respectively, which is consistent with the Raman results in terms of defect formation behavior. The detailed XPS results provide insights into the formation of oxygen functional groups in each step. During the thermal reduction of GO, most of the hydroxyl groups (—OH) were removed, while some of relatively thermostable oxygen groups including ether (C—O—C), carbonyl (C═O), and carboxyl (O═C—O) groups remained.[52] The remaining oxygen content slightly increased after the "punching" process as the edge hole was decorated with a small dose of the oxygen species by combustion of defects in air.

More functional groups were then introduced by acid treatment in Gr and HGr. Carbonyl (C═O) and ether (C—O—C) groups were found to be the main components of O-HGr, whereas O-Gr contained more carboxyl (O═C—O) groups. Given that different main functional

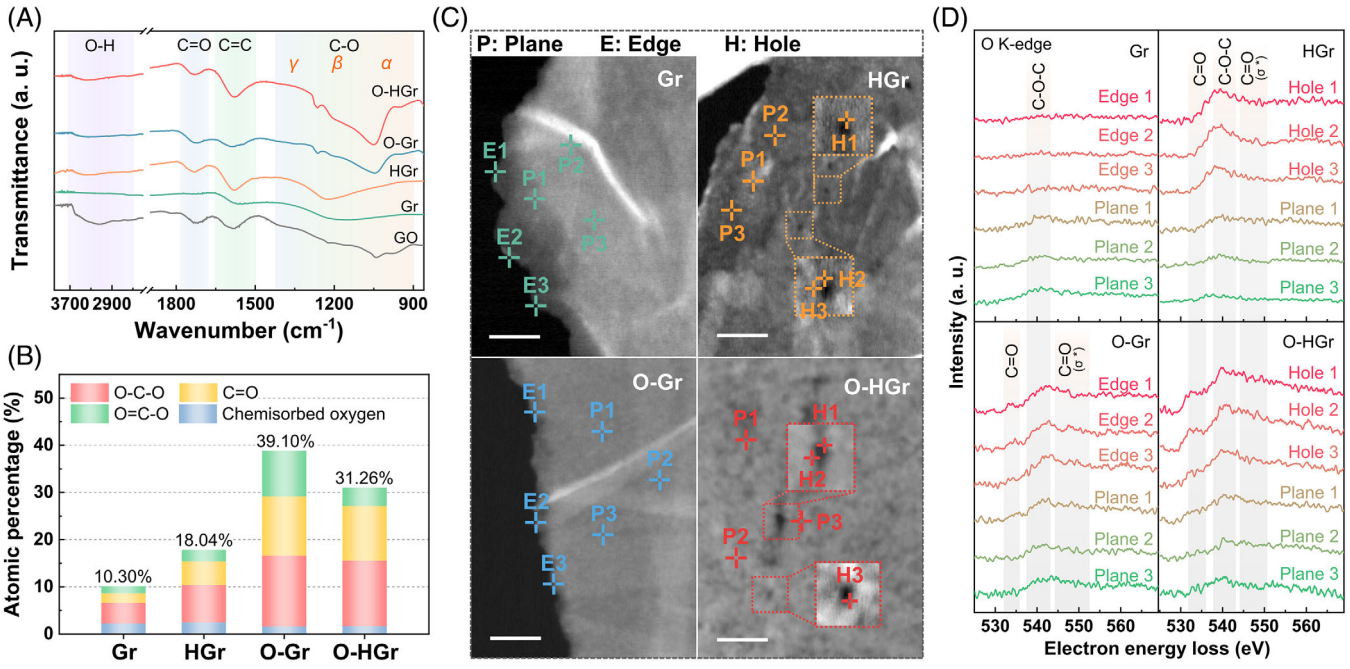

FIGURE 2 Structural characterization of graphene electrocatalysts. (A) FT-IR spectra of GO, Gr, HGr, O-Gr, and O-HGr. (B) Summarized oxygen contents derived by the high resolution of XPS C 1 s and O 1 s spectra of Gr, HGr, O-Gr, and O-HGr. (C) STEM images (scale bar: 25 nm). The cross marks on the images indicate the chosen regions for STEM-EELS measurement. The P, E, and H as alphabetic symbols represent plane, edge, and hole, respectively. (D) EELS spectra at the O K-edge for all samples

groups were formed between the two oxidized graphenes, we hypothesized that the edge holes of O-HGr were mostly enriched with carbonyl and ether functional groups, whereas the non-crystalline areas of O-Gr were dominated by carboxyl groups along with the other two functional groups. To verify this assumption, we investigated the local atomic configuration of oxygen using EELS spectra. Zones in the basal planes, edges, and holes were specifically selected for EELS measurements, as shown in the STEM images (Figure 2C) and the corresponding spectra at the O K-edge were presented in Figure 2D. All spectra showed average molecular orientation over all oxygen covalent bonds, which had distinct tensor natures, as is further discussed below. The spectra in the basal plane regions of Gr exhibited a negligible peaks from 540 to 550 eV, indicating a few remaining oxygen groups (as demonstrated by FT-IR and XPS analysis) that were not found around the edges of the Gr sheet. The spectra of the HGr basal planes showed no characteristic signals, similar to those of Gr. However, the spectra near the hole edges showed more apparent peaks between 533 and 550 eV, resulting mostly from ether (C—O—C) and for the rest from carbonyl (C═O) and carboxyl (O—C═O) groups.[53] Thus, it could be assumed that most oxygen functional groups were ether groups and concentrated in the hole edges of HGr. After acid treatment of Gr and HGr, we could further observe the different functional group formation derived by the structural distinction depending on the presence of the holes in the basal plane. On close examination of the spectra for O-HGr in the zone of the hole edges, a conspicuous signal was observed at approximately 532 and 539 eV, which can be attributed to the transition from the 1 s state to the π^* orbital originating predominantly in carbonyl and ether from vacancy defects[54,55] at the edges of the holes, respectively. These distinct signals became weak in the O-HGr plane spectra, further confirming that the ether-carbonyl couple is formed at the hole edges of O-HGr. As for O-Gr, while the plane spectra appeared similar with those of O-HGr, the edge ones presented relatively small peaks at 534.5 eV assigned to C═O π^* transition for carbonyl and carboxylic groups along with the σ^* signal between 545 and 552 eV.[55] Based on the structural analysis, the four distinct features of functional group formation for each graphene catalyst are expected to function differently to tailor ORR activity for H_2O_2 production.

We evaluated the electrochemical performance of the prepared electrocatalysts toward H_2O_2 production using the rotating ring disk electrode (RRDE) setups. The obtained polarization curves in alkaline (0.1 M KOH), neutral (0.1 M phosphate buffer solution [PBS]) and acidic (0.1 M $HClO_4$) conditions at various rotation rates are shown in Figure S8. The RRDE results in alkaline and neutral electrolytes and the corresponding H_2O_2 selectivity are shown in Figure 3A–C. In alkaline electrolyte, all the samples favored the $2e^-$ ORR. Performance comparison of Gr and HGr indicates that the hole edges produced by the removal of lattice defects are more active for H_2O_2 production, showing a higher $J_{H_2O_2}$ than the intrinsic defects in Gr for the entire active potential range (0.20–0.77 V). This enhanced performance of HGr should be due to the fact that the engineered edge sites have the proper adsorption and binding energies of intermediate (*OOH and *O).[49] A more detailed observation of the ORR results indicates that the hole edges of HGr are more advantageous as compared with the general defects of Gr, particularly in the kinetic region, with more positive onset potential value (~0.79 V vs. ~0.77 V) and greater H_2O_2 selectivity (~91% vs. ~87%). However, by gradually applying higher reduction potential, the ORR activity of HGr shifted slightly toward $4e^-$ ORR, with 85% selectivity at 0.2 V, whereas Gr showed better selectivity (88%–93%) below 0.6 V.

After further functionalization, the two oxidized samples induced different responses to the same functionalization condition for overall ORR activities. Despite good H_2O_2 selectivity (~90%) in the entire potential range (0.20–0.65 V), O-Gr showed degraded performance with higher overpotential with the onset potential value of ~0.65 V and low reduction current (0.95 mA cm^{-2} at 0.2 V). These unsatisfactory activities of O-Gr are due to the excessive oxygen content, which results in poor electron transport.[56] O-HGr, in contrast, showed more improved performance in comparison with O-Gr in $J_{H_2O_2}$ (2.45 mA cm^{-2} vs. 0.54 mA cm^{-2} at 0.4 V) with better H_2O_2 selectivity values (9%0–100%) in a wide potential range (0.20–0.77 V) and better onset potential value (~0.78 V vs. ~0.65 V). This outstanding selectivity over a wide potential range surpasses those of previously reported CBEs and non-carbon electrocatalysts (Figure S9), suggesting that our defect engineering is well suited for the selective $2e^-$ ORR.

In addition, the ORR performance in alkaline media for all the samples emerged consistently in the neutral electrolytes. The Gr electrocatalyst showed 77%–80% H_2O_2 selectivity and an onset potential value of 0.5 V. However, performance deteriorated after functionalization on the lattice defects of Gr. As mentioned earlier, even though certain oxygen functional groups can enhance overall selectivity, a surplus may act negatively by lowering conductivity,[56] resulting in higher overpotential and low reduction current for H_2O_2 production with O-Gr. In holey graphene samples, HGr exhibited a slight increase in H_2O_2 current compared with that of Gr. However, the proportion of the $4e^-$ pathway to the total current steadily increased with a potential sweep in

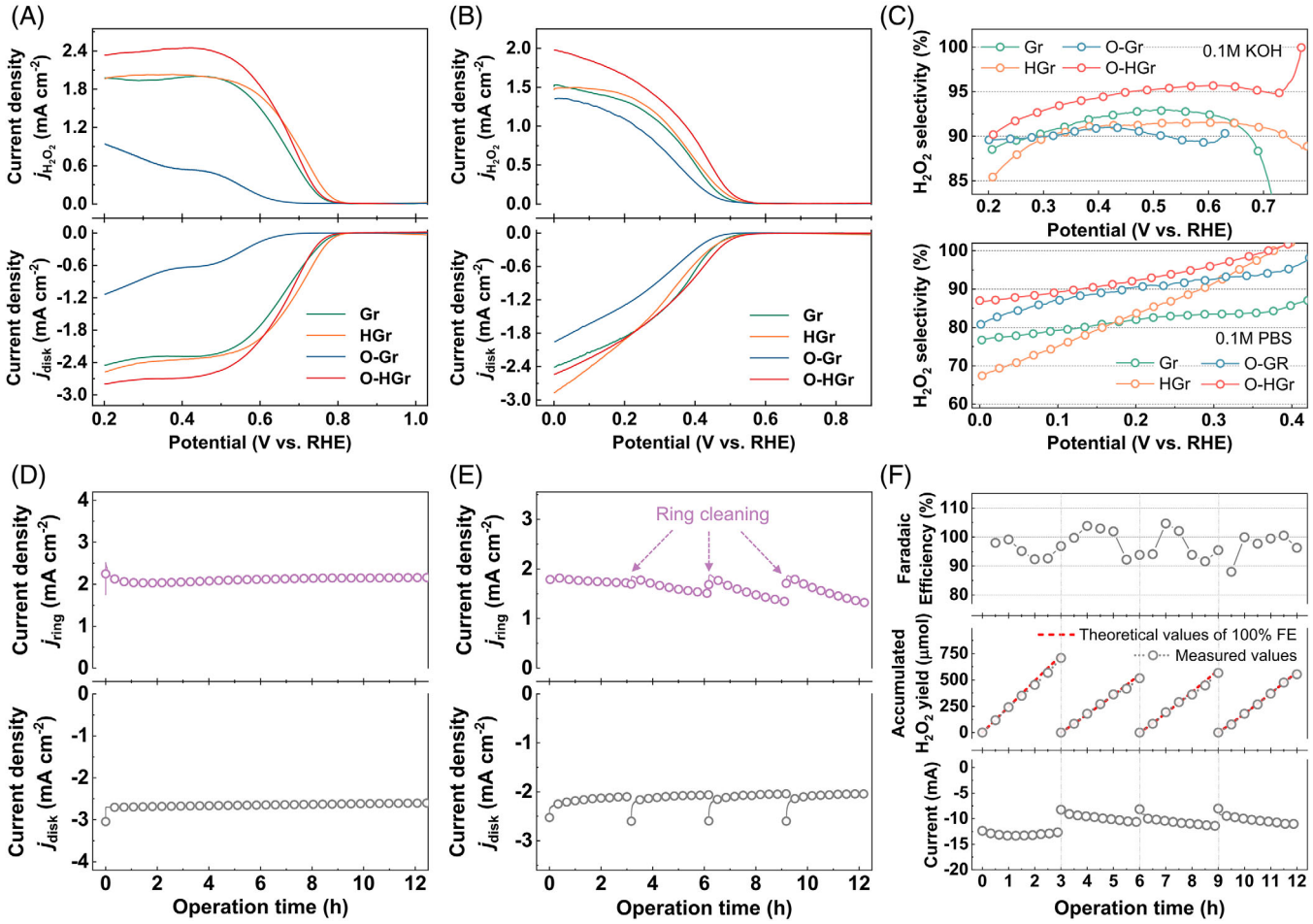

FIGURE 3 Electrochemical ORR performance of graphene electrocatalysts. Linear sweep voltammetry of RRDE measurements at 1600 rpm in (A) alkaline and (B) neutral electrolytes, and (C) corresponding H_2O_2 selectivity. Stability tests of O-HGr in (D) alkaline conditions at 0.3 V (vs. RHE) and (E) neutral conditions at 0.1 V (vs. RHE) for 12 h (ring electrode was cleaned every 3 h by rapid scan). (F) Bulk electrolysis production of H_2O_2 and stability performance of O-HGr catalyst using an H-cell test including CA curve, accumulated H_2O_2 yield, and the corresponding FE

the cathodic direction, showing a linear decrease of H_2O_2 selectivity from 100% to 66%. After oxidation, O-HGr delivered the most enhanced performance among the samples in overall electrocatalytic activities, with the earliest onset potential (0.56 V vs), highest ring current density (2 mA cm^{-2}), and enhanced H_2O_2 selectivity (87%–100%). These RRDE results suggest that among the different types of defects originated from each sample in this study, the combination of ether (C—O—C) and carbonyl (C═O) groups at the hole edges is the most active and selective configuration for 2e$^-$ ORR. In the case of acidic electrolyte, despite better activities of O-HGr than those of the other samples (Figure S10), the performance is not as good as those in the other electrolytes, which agrees well with the previous reports for CBEs.[35]

We then conducted the stability tests of O-HGr in both alkaline and neutral pH conditions using chronoamperometry (CA) measurements under constant potential (0.3 and 0.1 V for a disk electrode in alkaline and neutral media, respectively, and 1.2 V for a ring electrode), (Figure 3D and E). The results showed stable current output with ~96% current retention and nearly constant selectivity over a 12-hour testing period. Because the ring electrode can be affected by anion poisoning that decreases the ring current,[35] periodic electrochemical ring cleaning was performed in the neutral electrolyte. After that, the ring current recovered and overall current values were almost retained, indicating that the functionalized hole edge sites are stable in both alkaline and neutral conditions during electrochemical H_2O_2 production. We further evaluated the structural stability of O-HGr after long-term electrosynthesis using Raman analysis. A typical three-electrode cell configuration was used, and the working electrode was prepared with surface-enhanced Raman scattering (SERS) substrate (Figures S11A and B). The obtained CA curve

(Figure S12A) shows excellent durability of the O-HGr without current degradation. Raman and XPS spectra of before and after ORR (Figure S12 B–D) show negligible changes in the defect-related peaks including D and D′ bands and oxygen-related peaks, respectively. This small variation could be due to the absorbed O intermediates (O* and OOH*) at active sites of the graphene[57] rather than irreversible deformation of the structure, indicating the excellent electrocatalytic stability of the active sites of O-HGr. We further evaluated the morphologies after ORR using microscopic analysis (Figure S13). SEM images of the electrode surface and TEM results for individual O-HGr sheets exhibited insignificant changes in the overall morphologies, showing a well-maintained 2D sheet with microporosity.

We also used an H-type cell system (Figure S13) to investigate bulk electrosynthesis of H_2O_2 for more practical demonstration. A CA experiment for O-HGr was carried out for 12 h in an O_2-saturated 0.1 M KOH solution under constant potential (0.35 V). The electrolyte was replaced every 3 h due to the concentration change of the electrolyte by the generated H_2O_2. The H_2O_2 output was quantified every 30 min by a redox titration of cerium (IV) sulfate. The resulting UV absorption spectra, the polarization curve with the corresponding H_2O_2 yield, and the FE results are presented in Figure S16 and Figure 3F. The CA curves illustrate the outstanding retention of the reduction currents. The yields of H_2O_2 for each batch were calculated to be 2360, 1720, 1886, and 1843 mol Kg_{cat}^{-1} h^{-1}. Each yield was close to the theoretical values of 100% FE during the operation, even after 12 h. Collectively, the excellent stability and selectivity of O-HGr were confirmed by extensive testing, which suggests that O-HGr is a promising electrocatalyst for the direct synthesis of H_2O_2.

To elucidate another crucial role of the in-plain holes, we used an EIS system for the simultaneous determination of the charge transfer and mass transfer processes.[58] Mass transfer losses generally occur at high current density because of the sluggish mass transport of oxygen throughout active sites, resulting in limitations of the current production.[59] Because insufficient mass transport also causes product accumulation on the surface of electrocatalysts,[59] resulting in an undesirable extra reaction of H_2O_2 into H_2O, enhanced mass transport should be of greater importance for the $2e^-$ reaction. An appropriate equivalent circuit fitting (Figure S17) allowed for a reliable evaluation of the polarization resistance (R_p), which is the sum of the charge transfer resistance (R_{ct}) and diffusion (mass transfer) resistance (R_d).[58] To determine the contribution of R_{ct} and R_d to R_p in the three reduction potential regions, the kinetic region, the kinetic-diffusion mixed control region, and the mass transport region,[58] we analyzed R_p values with various rotation rates at three different potentials. The corresponding spectra and the calculated contribution of each resistance are shown in Figure S18. In the kinetic region for both O-Gr and O-HGr, the changes of R_p on the rotation rates appeared to be insignificant, which indicates that R_d is negligible in this region. The rotation rates effect on R_p was observed in the mixed kinetic-diffusion control region, showing a higher R_p at lower rotation rates, which was more noticeable in the mass transport region. This result suggests that the rotation rate has far more influence at a higher reduction potential, indicating that R_p would be dominated by R_d with potential sweep in the cathodic direction.

Based on the R_p evaluation, we examined the EIS for O-Gr and O-HGr over a wide potential range. The resulting values of R_p are plotted with the polarization curves (Figure 4C and D). The initial resistance progressively decreased as a lower potential was applied toward the kinetic-diffusion mixed control region because of the decrease in interfacial charge transfer. With a lower reduction potential in the mass transport region, the total R_p continuously increased, which is a result of the gradually increased R_d, while changes in R_{ct} were insignificant. When comparing the trends in R_p between both graphene, O-HGr has more efficient charge transfer and mass transport behavior than O-Gr does. On closer examination, the initial R_p values for O-HGr ranged from 1123 to 281 Ω, which were much lower than those of O-Gr (1636 to 819 Ω), indicating that O-HGr has more efficient charge transfer. This enhanced kinetic activity of O-HGr was further confirmed in Figure S19 which shows a higher kinetic current density of O-HGr than that of O-Gr. As the applied potential approached the diffusion-limited region, O-Gr exhibited a drastic increase in R_p to a value of 2512 Ω; conversely, O-HGr showed a relatively small resistance change (790 Ω), indicating that the holey graphene had much more efficient mass transport. In short, the EIS results confirm that the elaborate structural design of O-HGr promotes efficient ORR performance in both kinetic activities and mass transport properties.

DFT calculations were performed to elucidate the nature of the active sites responsible for the enhanced $2e^-$ ORR performance on our designed electrocatalyst. A two-dimensional graphene sheet was used as a model structure. To model the experimentally obtained pore sites using the "punching" process, a graphene model was established by removing a 7777–6-5555 defect. The unsaturated carbon sites on the defect are easily oxidized and form different oxygen functional groups. To simulate the possible active sites in the presence of the ether (C—O—C) and carbonyl (C═O) functional groups

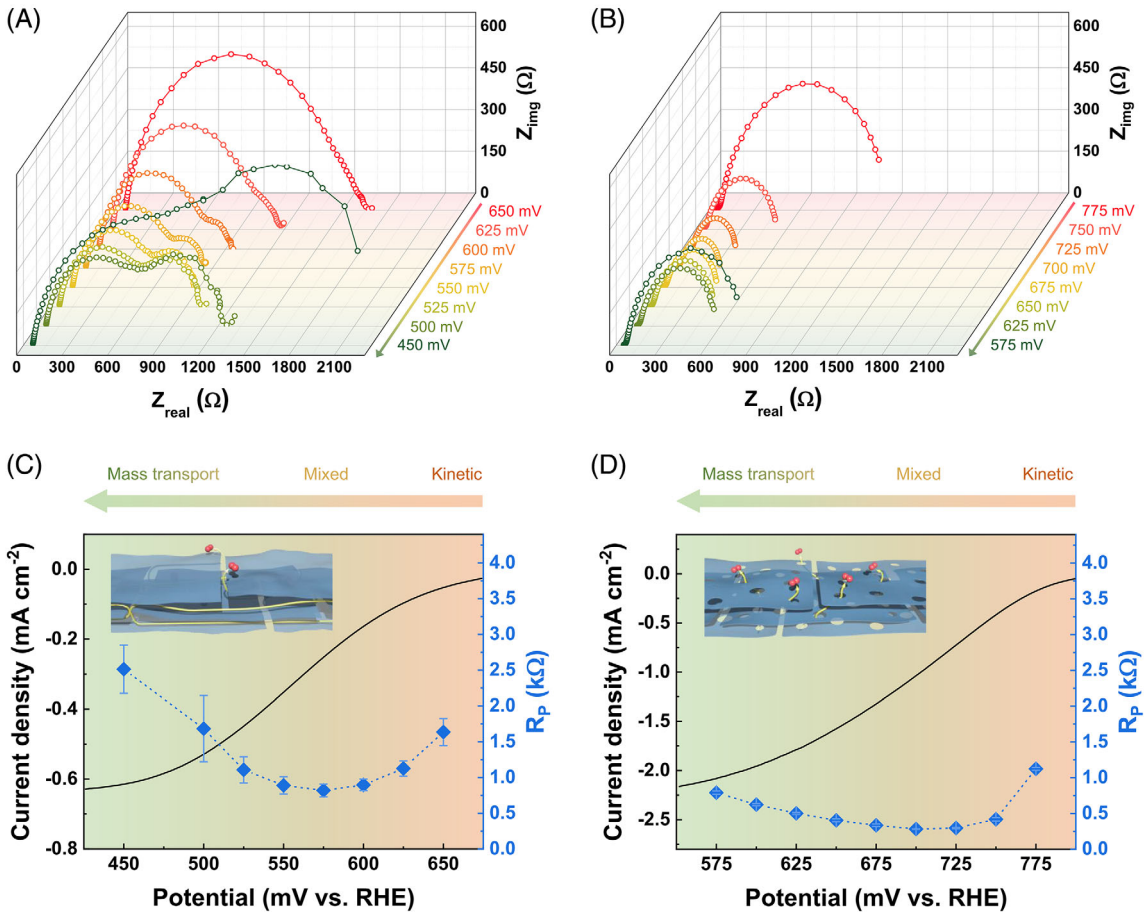

FIGURE 4 Kinetic activity and mass transport performance. Impedance spectra on a wide potential range for (A) O-Gr and (B) O-HGr and evaluated polarization resistance with the polarization curves for (C) O-Gr and (D) O-HGr

observed via FT-IR, XPS, and EELS analysis, several models were investigated, where both isolated and combined oxygen functional groups were included (Figure 5A). For the individual functional groups, we considered H-terminated hole models.

The $2e^-$ ORR process involves two coupled proton-electron transfer steps. The first one is transferring a coupled proton-electron to O_2 adsorbed at the catalyst surface to form HOO* (asterisk indicate a surface-bound species). The second is a subsequent proton-electron transfer to HOO* to form H_2O_2. Since both steps involve HOO* as an intermediate, adsorption free energy of HOO* can be successfully used as an activity descriptor for the $2e^-$ ORR.[60,61] Hence, the HOO* adsorption free energy was calculated in this work on the various possible active sites in each examined model structure (Figure S21). The most active sites (marked with black circles) in each structure are reported in Figure 5A. The $2e^-$ ORR activity was measured by calculating the limiting potential, U_L, which is defined as the maximum potential at which all elementary steps are downhill in free energy. Theoretical overpotential (OP) is defined as the difference between the equilibrium potential (0.70 V) and the limiting potential. Figure 5B displays the theoretical activity volcano, where the calculated limiting potential is plotted as a function of HOO* adsorption free energy. The pick of the volcano is positioned at the HOO* adsorption free energy of 4.22 eV, which corresponds to the maximum limiting potential (0.70 V) and zero overpotential. To the right side of the volcano ($\Delta G_{HOO^*} > 4.22$ eV), there are active sites with weak HOO* adsorption free energy, where the activity is limited by the first proton-electron transfer step, that is, formation of HOO*. These active sites preserve the O-O bond in HOO* intermediate and increase the selectivity toward H_2O_2. In contrast, to the left side of the volcano ($\Delta G_{HOO^*} < 4.22$ eV), there are active sites with strong HOO* adsorption free energy, where the activity is limited by protonation of HOO* to form H_2O_2, hence the selectivity is low. This analysis allows to underline the activity and selectivity trend across different active sites examined herein and pinpoint the most active functional

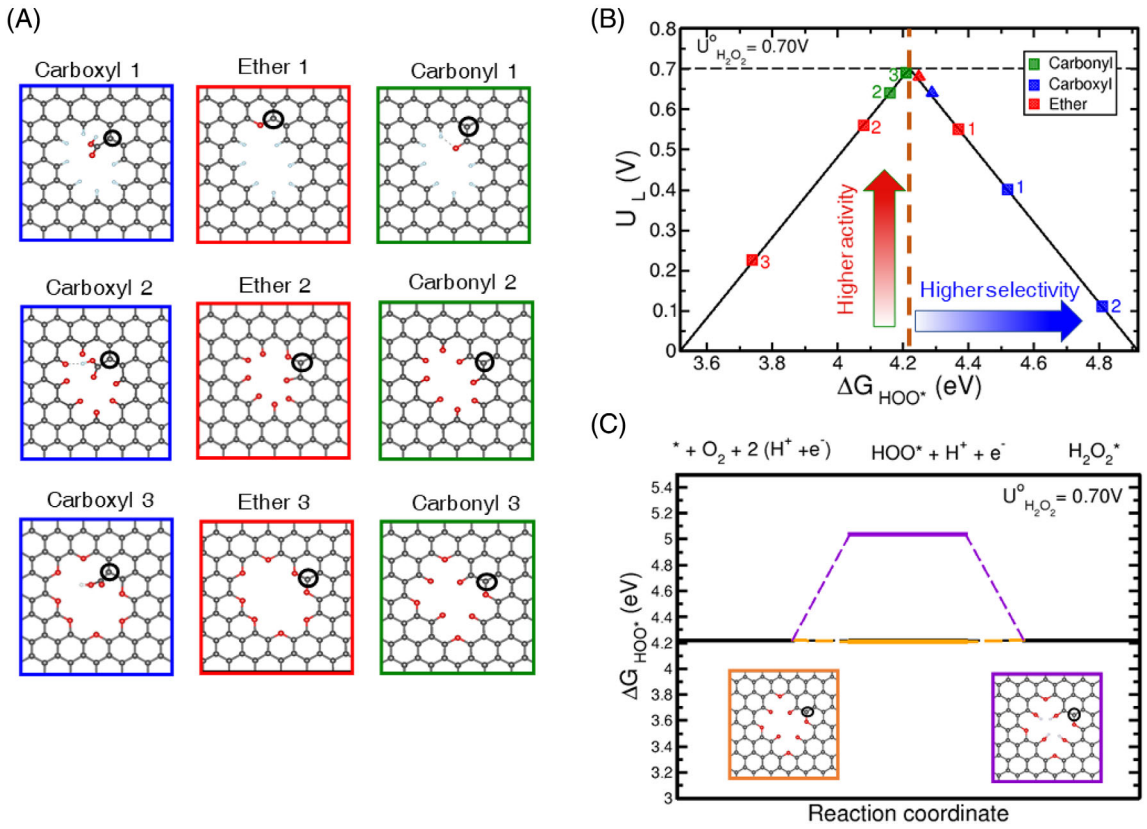

FIGURE 5 (A) Optimized geometry of holy graphene models including carboxyl (blue), etheric (red), and carbonyl (green) functional groups. Active sites are shown by black circles. (B) The $2e^-$ ORR activity volcano plot for the most active structures shown in 5a. The results of previously reported active functional groups are denoted in the activity volcano plot with triangles.[35] (C) Free energy diagram for $2e^-$ ORR on ether/carbonyl (orange) and ether/hydroxyl structures. The plot shows a large overpotential on the protonated model

groups. In the following, we summarize the key findings in three groups based on the type of oxygen functional groups, carboxyl, ether and carbonyl.

Structures with carboxyl functional group (Figure 5, blue squares) are located in the right side of the volcano with weak HOO* adsorption energy, high selectivity and low activity (OPs: 0.3 V and 0.6 V for carboxyl 1 and 2, respectively) toward H_2O_2. We note that, the activity of carboxyl on the edge and basal plane of the graphene was previously reported[35] where edge located carboxyl (Figure 5, blue triangle) was reported to be highly active (OP: 0.06 V) for H_2O_2 production. The basal plane carboxyl reported in the previous study was confined in a small pore and its activity is slightly more (OP: 0.14 V) than carboxyl confined in a large pore investigated herein (OP: 0.3 V).

Ether functional group (Figure 5, red squares) shows high activity (OP: 0.15 V) and selectivity toward H_2O_2 when it is isolated in a large pore size (Figure 5, ether 1). The previous report shows a high activity for the ether in a small pore (OP: 0.02 V).[35] Similar to carboxyl, ether functional group becomes slightly less active when pore size is increased. A saturated pore with ether configuration (ether 3) on the other hand, strongly adsorb HOO* which in turn results in decreased activity (OP: 0.48 V) and selectivity toward H_2O_2. The HOO* adsorption energy becomes weaker ($\Delta G_{HOO*} = 4.08$ eV) when ether is confined in a pore saturated with carbonyl functional group, and its activity is improved (OP: 0.14 V). However, its selectivity remains low because $\Delta G_{HOO*} < 4.22$ eV.

An isolated carbonyl (Carbonyl 1) has a very weak HOO* adsorption energy, and its data point is not showing up in the activity volcano. On the other hand, a pore structure saturated with carbonyl functional group (Carbonyl 2) (Figure 5, green) shows stronger HOO* adsorption energy (4.16 eV) which places it in the region with low selectivity but near the peak of the activity volcano (OP: 0.06 V). Lastly, a pore structure saturated with an alternative combination of carbonyl and ether (Carbonyl 3) (Figure 5, green) show the maximum activity with nearly zero OP suggesting a synergistic effect between these two functional groups.

Using DFT calculations we also investigated the reason behind the activity drop in acidic and neutral media which was detected by RRDE analysis (Figure 3B). One

possible hypothesis is that the nature of active site changes because there are more abundant protons in the neutral solution, which may protonate carbonyl oxygen functional groups and form hydroxyl. To determine the effects of protonation of the oxygen functional groups on the $2e^-$ ORR activity, we compared the following two model structures: combined carbonyl/ether, which is the most active structure, and combined hydroxyl/ether on the pore. Figure 5C shows the results in a free-energy diagram. The ideal catalyst (black line) follows a flat adsorption free energy at U = 0.70 V. As predicted by the activity volcano plot (Figure 5B), carbonyl/ether activity is very close to the ideal catalyst. However, taking the same carbon atom as the active site, a large overpotential is observed in the hydroxyl/ether model. To better understand this behavior, we performed a Bader charge analysis for each structure (Table S1). These results showed the active site on hydroxyl/ether model was negatively charged compared to carbonyl/ether model. Negative charge accumulation resulted in a repulsive interaction between HOO* and surface which results in higher activation barrier for the reaction. We conclude the high selectivity and activity in alkaline media is a result of coordination between carbonyl and ether functional groups at pore site. On the other hand, functional group hydrogenation in acidic and neutral media increases the $2e^-$ ORR reaction barrier by charge redistribution on the active site.

3 | CONCLUSION

In summary, by combining experimental and theoretical analysis, we demonstrated a tactical approach for the defect engineering of graphene using a punching and functionalization process for enhanced H_2O_2 electrosynthesis via $2e^-$ ORR. HR-TEM results revealed that an oxidized hole with an average diameter of ~2 nm formed in the basal plane of graphene. The well-characterized FT-IR, XPS, and EELS results indicate that the specific functional groups of ether (C—O—C) and carbonyl (C═O) formed at the hole edges. This unique structure of O-HGr allowed fine modulation of the overall ORR activity for highly selective H_2O_2 production. When comparing the ORR performance of O-HGr with that of the other control samples, a combination of two different oxygen functional groups was identified as the major active sites for highly active and selective H_2O_2 production, exhibiting an average of 95% H_2O_2 selectivity and ~97% FE for bulk electrosynthesis in the alkaline electrolyte. EIS analysis further uncovered another vital role of the hole, showing improved diffusion efficiency of oxygen with significantly lower resistance for both kinetic charge transfer and mass transport compared with non-holey graphene. DFT calculations suggested that a combination of functional groups, such as ether and carbonyl, provides the necessary active site to achieve maximum activity toward H_2O_2 production. The calculations also revealed a large overpotential at lower pH values because of the protonation of oxygen functional group, which explains the performance drop in neutral media. This study provides a general approach for the defect engineering of CBEs through a proper understanding of active sites in the ORR process.

4 | METHOD

4.1 | Preparation of Gr, HGr, O-Gr, and O-HGr

GO was prepared as a starting material using a modified Hummers' method. A 10 g of graphite was added to 380 ml of sulfuric acid (H_2SO_4) with mild stirring followed by adding 50 g of potassium permanganate ($KMnO_4$). The mixture was subjected to constant stirring for 12 h at 35°C. After cooling down the mixture to 5°C, 500 ml of H_2O was slowly added as a quenching step. A 15 ml of H_2O_2 was then added until the color of the mixture turned golden yellow, confirming the termination of the reaction. Finally, the GO was washed with 1 M HCl and then acetone, followed by drying at 60°C for 12 h, to obtain GO powder. We performed inductively coupled plasma optical emission spectroscopy to analyze metal residues in the as-prepared GO. The result indicates that GO does not include significant amount of metal impurities with the values of less than 0.0001 wt % for elements of iron, manganese, cobalt, and nickel. A 200 mg of Gr was produced by heat treatment of 500 mg of the GO powder at 500 °C in argon gas for 2 h with a ramp rate of 20°C min^{-1}. After the reduction of GO, there is no more significant weight loss in the following process. To prepare HGr, the obtained Gr powder was further heated in air with a ramp rate of 10°C min^{-1} and isothermally held at 410°C for 2 h. The acid treatment of the obtained graphenes was adopted to introduce the specific oxygen groups. In detail, both graphenes were immersed in 20 ml of 10 M HNO_3 with mild stirring for 10 min followed by moderate bath sonication in a sealed reactor for 5 min. The mixtures were slowly heated to 90 °C and then refluxed for 6 h. The acid-treated graphenes were washed with 200 ml of DI water three times and then with 50 ml of ethanol. The final products of O-HGr and O-Gr could be obtained after drying at 60°C for 12 h.

4.2 | Characterization

The typical morphologies of Gr, HGr, O-Gr, and O-HGr were characterized by SEM (S4800, Hitachi, Japan) at

15 kV and TEM (FEI, Titan G2 Cube 60–300) which is equipped with an image Cs corrector and operated at an accelerating voltage of 80 kV of which value is below critical energy predicted for severe knock-on damage on carbon nanostructures. The TEM is also equipped with a monochromator which enables to improve the attainable energy resolution of EELS with a spherical aberration corrected STEM. An energy filter of Quantum 963 was employed to support the high collection angles required for atomic column resolution EELS analysis. The Raman spectra were acquired by a Renishaw inVia with a 532-nm laser source. XPS measurements were performed with an XPS spectrometer (Thermo Fisher Scientific, Theta probe) using a monochromic Al Ka radiation X-ray source. FT-IR analyses were carried out using a Thermo Fisher Scientific Co. Nicolet 6700 with KBr pellets. A UV–vis spectrometer (Analytik Jena, Specord200) was used to obtain the UV–vis absorption between 300 and 800 nm at a resolution of 1 nm. TGA was taken by a simultaneous TGA/DTA/DSC analyzer (TA Instruments, SDTQ600).

4.3 | Electrochemical measurements

Electrochemical analyses, including cyclic voltammetry (CV), linear sweep voltammetry (LSV), and EIS, were carried out using a rotating disk electrode (RDE) setup and chronoamperometry (used to evaluate the ORR activity and stability of the prepared catalysts) using RRDE with a computer-controlled potentiostat (VSP, Bio-Logic SAS instrument, France) with a typical three-electrode cell possessing a gas flow system. These tests were performed in an O_2-saturated three-electrolyte solution (0.1 M KOH, 0.1 M PBS), or (0.1 M $HClO_4$) at 25°C. The background current was measured in N_2-saturated electrolytes. A platinum wire and a graphite rod were used as the counter electrodes for RRDE and H-cell test, respectively, whereas Ag/AgCl (acid and neutral electrolytes) and Hg/HgO (alkaline electrolyte) were used as the reference electrodes. The working electrodes were prepared by drop-casting 10 µl of the prepared sample suspensions (1 mg mL^{-1}) in a mixture of Mili-Q water and isopropanol solution (4:1) with 10 µl of Nafion (5%) onto the glassy carbon electrode (GC, 5-mm diameter, Pine Instrument Co.). For the EIS analysis, the impedance spectra were recorded with an AC amplitude of 5 mV in a frequency range of 100 kHz to 0.02 Hz using a single sine mode. The impedance spectra were fitted using ZFit fitting tools of EC-Lab software. The RDE and RRDE tests were performed with an electrode rotator (modulated speed rotator, Pine Instrument Co.), whereas the potential of the Pt ring electrode was held at 1.2 V (vs. RHE) to obtain the oxidation current of the as-formed H_2O_2. The total electron transfer number (n) and the selectivity of H_2O_2 were calculated using the following Equations (1) and (2):

$$H_2O_2\,(\%) = 200 \times \frac{I_R/N}{I_D + I_R/N}, \tag{1}$$

$$n = \frac{4\,|\,I_D\,|}{I_D + I_R/N}. \tag{2}$$

where I_R and I_D are the ring and disk current, respectively; N is the collection efficiency, which was calibrated to be 0.265. The following Levich equation (Equations (3) and (4)) was used to extract the kinetic current (j_{kin}) by correcting the mass transport losses:

$$\frac{1}{j} = \frac{1}{j_{kin}} + \frac{1}{j_{diff}} = \frac{1}{j_{kin}} + \frac{1}{B \cdot \sqrt{\omega}}. \tag{3}$$

$$B = 0.62 \cdot n \cdot F \cdot D_{O_2}^{2/3} \cdot \nu^{-1/6} \cdot C_{O_2}. \tag{4}$$

where j is the current density consisting of kinetic current (j_{kin}) and the diffusion current (j_{diff}), ω is the electrode rotation speed (rad s^{-1}), n is the number of electrons transferred during the reaction, D_{O_2} is the diffusion coefficient of oxygen in the electrolyte at 298 K (1.85×10^{-5} cm^2 s^{-1}), C_{O_2} is the oxygen concentration (1.21×10^{-6} mol cm^{-3}), F is the Faraday constant (96 485 $Cmol^{-1}$), and ν is the kinematic viscosity of oxygen (0.89×10^{-2} cm^2 s^{-1}). Bulk electrosynthesis of H_2O_2 was performed in alkaline electrolyte to further confirm the selectivity and determine the amount of H_2O_2 using a two-compartment H-type cell with a Nafion membrane as the separator (Figure S14). Each chamber was filled with 15 ml of electrolyte (0.1 M KOH), and an inhibitor of 10 mM ethylenediaminetetraacetic acid (EDTA) was added to prevent H_2O_2 decomposition in alkaline media. In one chamber, the working electrode, reference electrode (Hg/HgO), and gas tube were placed; a counter electrode (graphite rod) was placed in the other chamber to prevent the oxidation of the H_2O_2 product. The electrolyte of the cathode compartment was saturated with pure oxygen gas and vigorously stirred to facilitate mass transport to the electrocatalyst surface. The working electrode was prepared by placing Teflon-treated carbon paper (1 cm × 1 cm) in electrocatalyst ink with sonication for 10 min and then drying the sample at 60°C. A chronoamperometric method was used to demonstrate the bulk electrosynthesis of H_2O_2 to simulate practical applications. A titration method with ceric sulfate was used to determine H_2O_2 concentration in the electrolyte through

the reaction of ($2Ce^{4+} + H_2O_2 \rightarrow 2Ce^{3+} + 2H^+ + O_2$). The calibrated slope was obtained by the UV–vis spectra at 317 nm for the standard titration solution of $Ce(SO_4)_2$ with various concentrations from 0.0 to 0.5 mM. (Figure S14) Samples of the electrolyte (10 μl) from the cathodic reaction were taken every 30 min during the operation time and then titrated with the yellow-colored Ce^{4+} solution. The resultant electrolyte samples gradually turned colorless as more Ce^{4+} was reduced by H_2O_2 to Ce^{3+}. This color transition was accurately measured by UV–vis spectroscopy to derive the H_2O_2 concentration (Figure S16). Quantification of H_2O_2 using the above titration method is based on the following equations.

$$\text{Accumulated } H_2O_2 \text{ concentration (mM)} = \frac{V_{\text{t, before}} \times [Ce^{4+}]_{\text{before}} - V_{\text{t, after}} \times [Ce^{4+}]_{\text{after}}}{\text{Overall charge passed (C)}}, \quad (5)$$

where $V_{\text{t,before}}$ and $V_{\text{t,after}}$ are the volumes of titration solution before and after adding the aliquot of electrolyte, respectively. $[Ce^{4+}]_{\text{before}}$ and $[Ce^{4+}]_{\text{after}}$ are the Ce^{4+} concentration (mM) before and after adding the aliquot of electrolyte, respectively.

$$\text{Accumulated } H_2O_2 \text{ yield (μmol)} = [H_2O_2]_{\text{after}} \times V_{\text{after}} - [H_2O_2]_{\text{before}} \times V_{\text{before}} \quad (6)$$

$$\text{Faradaic Efficiency of } H_2O_2 = \frac{\text{accumulated } H_2O_2 \text{ yield (mol)} \times \frac{2 \text{ mol e}^-}{1 \text{ mol } H_2O_2} \times \frac{96485 \text{ C}}{1 \text{ mol e}^-}}{\text{Overall charge passed (C)}} \times 100\%, \quad (7)$$

where V_{before} and V_{after} are the volumes of electrolyte before and after the aliquot sampling, respectively. And $[H_2O_2]_{\text{before}}$ and $[H_2O_2]_{\text{after}}$ are the cumulative H_2O_2 concentration before and after the aliquot sampling, respectively.

4.4 | Computational method

The DFT simulations were performed using Atomic Simulation Environment (ASE).[62] All electronic structure relaxations were performed via Quantum Espresso program package.[6] The electronic wave functions were expanded in plane waves with an optimized cutoff energy of 500 eV, while a 5000 grid was used for electronic density representation. Structures were modeled using a two-dimensional graphene layer with a fairly large unit cell of 9 × 9. The periodic images were separated using 18 Å vacuum. The Brillouin zone was sampled using gamma points. Supplementary Figure S20 (A and B) shows the convergence test for the *k*-point and vacuum size.

AUTHOR CONTRIBUTIONS

Zheng Chen, Tae Hee Han, and Ki Hwan Koh conceptualized the project and designed the experiment. Ki Hwan Koh performed all experimental works. Ki Hwan Koh carried out electrochemical evaluations and analyzed the results with the help of Qiaowan Chang and Yu Joong Kim. Samira Siahrostami and Amir Hassan Bagherzadeh Mostaghim designed and conducted DFT calculations. Ki Hwan Koh, Amir Hassan Bagherzadeh Mostaghim, Samira Siahrostami, Tae Hee Han, and Zheng Chen wrote the manuscript with the discussion with all authors. Zheng Chen and Tae Hee Han supervised the whole project.

ACKNOWLEDGMENTS

Z.C. acknowledges the support from the ACS Petroleum Research Fund (#59989-DNI5) and Jacob School of Engineering at UC San Diego. T.H.H. and K.K.H. would like to thank the Basic Science Research Program through the National Research Foundation of Korea (2020R1A2C2101652). S.S. and A.H.B.M. acknowledge the support from the University of Calgary's Canada First Research Excellence Fund Program, the Global Research Initiative in Sustainable Low Carbon Unconventional Resources.

CONFLICT OF INTEREST

The authors declare no conflict of interest.

DATA AVAILABILITY STATEMENT

Research data are not shared.

ORCID

Samira Siahrostami https://orcid.org/0000-0002-1192-4634
Tae Hee Han https://orcid.org/0000-0001-5950-7103
Zheng Chen https://orcid.org/0000-0002-9186-4298

REFERENCES

1. Freakley SJ, He Q, Harrhy JH, et al. Palladium-tin catalysts for the direct synthesis of H_2O_2 with high selectivity. *Science*. 2016; 351(6276):965-968. doi:10.1126/science.aad5705
2. Yang S, Verdaguer-Casadevall A, Arnarson L, et al. Toward the decentralized electrochemical production of H_2O_2: a focus on the catalysis. *ACS Catal*. 2018;8(5):4064-4081. doi:10.1021/acscatal.8b00217
3. Campos-Martin JM, Blanco-Brieva G, Fierro JLG. Hydrogen peroxide synthesis: an outlook beyond the anthraquinone process. *Angew Chem Int Ed*. 2006;45(42):6962-6984. doi:10.1002/anie.200503779

4. Jiang Y, Ni P, Chen C, et al. Selective electrochemical H_2O_2 production through two-electron oxygen electrochemistry. *Adv Energy Mater*. 2018;8(31):1801909. doi:10.1002/aenm.201801909
5. Melchionna M, Fornasiero P, Prato M. The rise of hydrogen peroxide as the main product by metal-free catalysis in oxygen reductions. *Adv Mater*. 2018;31(13):1802920.
6. Verdaguer-Casadevall A, Deiana D, Karamad M, et al. Trends in the electrochemical synthesis of H_2O_2: enhancing activity and selectivity by electrocatalytic site engineering. *Nano Lett*. 2014;14(3):1603-1608. doi:10.1021/nl500037x
7. Siahrostami S, Villegas SJ, Bagherzadeh Mostaghimi AH, et al. A review on challenges and successes in atomic-scale design of catalysts for electrochemical synthesis of hydrogen peroxide. *ACS Catal*. 2020;10(14):7495.
8. Jiang K, Zhao J, Wang H. Catalyst design for electrochemical oxygen reduction toward hydrogen peroxide. *Adv Funct Mater*. 2020;30(35):2003321. doi:10.1002/adfm.202003321
9. Zhang J, Zhang H, Cheng M-J, Lu Q. Tailoring the electrochemical production of H_2O_2: strategies for the rational Design of High-Performance Electrocatalysts. *Small*. 2020;16(15):1902845. doi:10.1002/smll.201902845
10. Kim JH, Kim Y-T, Joo SH. Electrocatalyst design for promoting two-electron oxygen reduction reaction: Isolation of active site atoms. *Curr Opin in Electrochem*. 2020;21:109-116.
11. Shen R, Chen W, Peng Q, et al. High-concentration single atomic Pt sites on hollow CuSx for selective O_2 reduction to H_2O_2 in acid solution. *Chem*. 2019;5(8):2099-2110. doi:10.1016/j.chempr.2019.04.024
12. Choi CH, Kim M, Kwon HC, et al. Tuning selectivity of electrochemical reactions by atomically dispersed platinum catalyst. *Nat Comm*. 2016;7(1):10922. doi:10.1038/ncomms10922
13. Kim JH, Shin D, Lee J, et al. A general strategy to atomically dispersed precious metal catalysts for unravelling their catalytic trends for oxygen reduction reaction. *ACS Nano*. 2020;14(2):1990-2001. doi:10.1021/acsnano.9b08494
14. Yang S, Kim J, Tak YJ, Soon A, Lee H. Single-atom catalyst of platinum supported on titanium nitride for selective electrochemical reactions. *Angew Chem Int Ed*. 2016;55(6):2058-2062.
15. Sahoo SK, Ye Y, Lee S, et al. Rational design of TiC-supported single-atom electrocatalysts for hydrogen evolution and selective oxygen reduction reactions. *ACS Energy Lett*. 2018;4(1):126-132.
16. Abbott DF, Mukerjee S, Petrykin V, et al. Oxygen reduction on nanocrystalline ruthenia: local structure effects. *RSC Adv*. 2015;5(2):1235-1243. doi:10.1039/C4RA10001H
17. Zheng Z, Ng YH, Wang D-W, Amal R. Epitaxial growth of Au-Pt-Ni Nanorods for direct high selectivity H_2O_2 Production. *Adv Mater*. 2016;28(45):9949-9955. doi:10.1002/adma.201603662
18. Jirkovský JS, Panas I, Ahlberg E, Halasa M, Romani S, Schiffrin DJ. Single atom hot-spots at Au–Pd Nanoalloys for Electrocatalytic H_2O_2 Production. *J Am Chem Soc*. 2011;133(48):19432-19441. doi:10.1021/ja206477z
19. Pizzutilo E, Kasian O, Choi CH, et al. Electrocatalytic synthesis of hydrogen peroxide on Au-Pd nanoparticles: from fundamentals to continuous production. *Chem Phys Lett*. 2017;683(1):436-442. doi:10.1016/j.cplett.2017.01.071
20. Huang J, Chen J, Fu C, et al. 2D Hybrid of Ni-LDH chips on carbon nanosheets as cathode of Zinc–air battery for electrocatalytic conversion of O_2 into H_2O_2. *ChemSusChem*. 2020;13(6):1496-1503.
21. Sheng H, Hermes ED, Yang X, et al. Electrocatalytic production of H_2O_2 by selective oxygen reduction using earth-abundant cobalt pyrite (CoS_2). *ACS Catal*. 2019;9(9):8433-8442. doi:10.1021/acscatal.9b02546
22. Zhao W-W, Bothra P, Lu Z, et al. Improved Oxygen Reduction Reaction Activity of Nanostructured CoS_2 through Electrochemical Tuning. *ACS Appl Energy Mater*. 2019;2(12):8605-8614.
23. Gao J, Yang HB, Huang X, et al. Enabling direct H_2O_2 production in acidic media through rational design of transition metal single atom catalyst. *Chem*. 2020;6(3):658-674. doi:10.1016/j.chempr.2019.12.008
24. Jiang K, Back S, Akey AJ, et al. Highly selective oxygen reduction to hydrogen peroxide on transition metal single atom coordination. *Nat Comm*. 2019;10(1):3997. doi:10.1038/s41467-019-11992-2
25. Jung E, Shin H, Lee B-H, et al. Atomic-level tuning of Co–N–C catalyst for high-performance electrochemical H_2O_2 production. *Nat Mater*. 2020;19(4):436-442.
26. Li B-Q, Zhao C-X, Liu J-N, Zhang Q. Electrosynthesis of hydrogen peroxide synergistically catalyzed by atomic Co–N_x–C sites and oxygen functional groups in noble-metal-free Electrocatalysts. *Adv Mater*. 2019;31(35):1808173. doi:10.1002/adma.201808173
27. Sun Y, Silvioli L, Sahraie NR, et al. Activity–selectivity trends in the electrochemical production of hydrogen peroxide over single-site metal–nitrogen–carbon catalysts. *J Am Chem Soc*. 2019;141(31):12372-12381.
28. Tang C, Jiao Y, Shi B, et al. Coordination tunes selectivity: two-electron oxygen reduction on high-loading molybdenum single-atom catalysts. *Angew Chem Int Ed*. 2020;59(23):9171-9176. doi:10.1002/anie.202003842
29. Chen S, Chen Z, Siahrostami S, et al. Designing boron Nitride Islands in carbon materials for efficient electrochemical synthesis of hydrogen peroxide. *J Am Chem Soc*. 2018;140(25):7851-7859. doi:10.1021/jacs.8b02798
30. Chen S, Chen Z, Siahrostami S, et al. Defective carbon-based materials for the electrochemical synthesis of hydrogen peroxide. *ACS Sustainable Chem Eng*. 2017;6(1):311-317.
31. Fellinger T-P, Hasche F, Strasser P, Antonietti M. Mesoporous nitrogen-doped carbon for the Electrocatalytic synthesis of hydrogen peroxide. *J Am Chem Soc*. 2012;134(9):4072-4075. doi:10.1021/ja300038p
32. Han G-F, Li F, Zou W, et al. Building and identifying highly active oxygenated groups in carbon materials for oxygen reduction to H_2O_2. *Nat Comm*. 2020;11(1):2209. doi:10.1038/s41467-020-15782-z
33. Iglesias D, Giuliani A, Melchionna M, et al. N-doped graphitized carbon Nanohorns as a forefront Electrocatalyst in highly selective O_2 reduction to H_2O_2. *Chem*. 2018;4(1):106-123. doi:10.1016/j.chempr.2017.10.013
34. Kim HW, Ross MB, Kornienko N, et al. Efficient hydrogen peroxide generation using reduced graphene oxide-based oxygen reduction electrocatalysts. *Nat Catal*. 2018;1(4):282-290. doi:10.1038/s41929-018-0044-2
35. Lu Z, Chen G, Siahrostami S, et al. High-efficiency oxygen reduction to hydrogen peroxide catalysed by oxidized carbon materials. *Nat Catal*. 2018;1(2):156-162.
36. Chang Q, Zhang P, Mostaghimi AHB, et al. Promoting H_2O_2 production via 2-electron oxygen reduction by coordinating

partially oxidized Pd with defect carbon. *Nat Comm*. 2020;11(1):2178. doi:10.1038/s41467-020-15843-3

37. Sun Y, Li S, Jovanov ZP, et al. Structure, activity, and faradaic efficiency of nitrogen-doped porous carbon catalysts for direct electrochemical hydrogen peroxide production. *ChemSusChem*. 2018;11(19):3388-3395. doi:10.1002/cssc.201801583
38. Sun Y, Sinev I, Ju W, et al. Efficient electrochemical hydrogen peroxide production from molecular oxygen on nitrogen-doped mesoporous carbon catalysts. *ACS Catal*. 2018;8(4):2844-2856. doi:10.1021/acscatal.7b03464
39. Banhart F, Kotakoski J, Krasheninnikov AV. Structural defects in graphene. *ACS Nano*. 2011;5(1):26-41. doi:10.1021/nn102598m
40. Yan X, Jia YJ, Yao X. Defects on carbons for electrocatalytic oxygen reduction. *Chem Soc Rev*. 2018;47(20):7628-7658. doi:10.1039/C7CS00690J
41. Jia Y, Zhang L, Du A, et al. Defect graphene as a trifunctional catalyst for electrochemical reactions. *Adv Mater*. 2016;28(43):9532-9538. doi:10.1002/adma.201602912
42. Zhang L, Xu Q, Niu J, Xia Z. Role of lattice defects in catalytic activities of graphene clusters for fuel cells. *Phys Chem Chem Phys*. 2015;17(26):16733-16743. doi:10.1039/C5CP02014J
43. Zhao H, Sun C, Jin Z, et al. Carbon for the oxygen reduction reaction: a defect mechanism. *J Mater Chem A*. 2015;3(22):11736-11739. doi:10.1039/C5TA02229K
44. Xu L, Lixue J, Zhengju Z, et al. Wet-chemistry grafted active pyridinic nitrogen sites on holey graphene edges as high performance ORR electrocatalyst for Zn-Air batteries. *Mater Today Energy*. 2019;11:24-29.
45. Karolina K, Lixue J, Kaicai F, et al. Two-step activated carbon cloth with oxygen-rich functional groups as a high-performance additive-free air electrode for flexible zinc–air batteries. *Adv Energy Mater*. 2019;9(4):1802936.
46. Gurzęda B, Buchwald T, Nocuń M, Bąkowicz A, Krawczyk P. Graphene material preparation through thermal treatment of graphite oxide electrochemically synthesized in aqueous sulfuric acid. *RSC Adv*. 2017;7(32):19904-19911.
47. Ralph Y, Chor W. Kinetics and mechanism of oxidation of basal plane on graphite. *J Chem Phys*. 1981;75(9):4471-4476.
48. Amedeo Bellunato B, Hadi Arjmandi T, Yanina C, Grégory S. Chemistry at the edge of graphene. *ChemPhysChem*. 2015;17(6):785-801.
49. Huajie Y, Zhiong T. Ultrathin two-dimensional layered metal hydroxides: an emerging platform for advanced catalysis, energy conversion and storage. *Chem Soc Rev*. 2016;45(18):4873-4891. doi:10.1039/C6CS00343E
50. Huajie Y, Yuhai D, Shan C, Zhengju Z, Porun L, Huijun Z. 2D Electrocatalysts for converting earth-abundant simple molecules into value-added commodity chemicals: recent Progress and perspectives. *Adv Mater*. 2020;32(18):1904870. doi:10.1002/adma.201904870
51. Krishna R, Wade J, Jones AN, Lasithiotakis M, Mummery PM, Marsden BJ. An understanding of lattice strain, defects and disorder in nuclear graphite. *Carbon*. 2017;124:314-333. doi:10.1016/j.carbon.2017.08.070
52. Acik M, Lee G, Mattevi C, et al. The role of oxygen during thermal reduction of graphene oxide studied by infrared absorption spectroscopy. *J Phys Chem C*. 2011;115(40):19761-19781. doi:10.1021/jp2052618
53. D'Angelo D, Bongiorno C, Amato M, et al. Electron energy-loss spectra of graphene oxide for the determination of oxygen functionalities. *Carbon*. 2015;93:1034-1041. doi:10.1016/j.carbon.2015.06.025
54. D'Angelo D, Bongiorno C, Amato M, et al. Oxygen functionalities evolution in thermally treated graphene oxide featured by EELS and DFT calculations. *J Phys Chem C*. 2017;121(9):5408-5414. doi:10.1021/acs.jpcc.7b00239
55. Ganguly A, Sharma S, Papakonstantinou P, Hamilton J. Probing the thermal deoxygenation of graphene oxide using high-resolution in situ X-ray-based spectroscopies. *J Phys Chem C*. 2011;115(34):17009-17019. doi:10.1021/jp203741y
56. Santosh Kumar B, Peter C, Paul J, Pagona P. Oxygen reduction reaction by electrochemically reduced graphene oxide. *Faraday Discuss*. 2014;173(0):415-428.
57. Yang HB, Miao J, Hung S-F, et al. Identification of catalytic sites for oxygen reduction and oxygen evolution in N-doped graphene materials: development of highly efficient metal-free bifunctional electrocatalyst. *Sci Adv*. 2016;2(4):e1501122. doi:10.1126/sciadv.1501122
58. Singh RK, Devivaraprasad R, Kar T, Chakraborty A, Neergat M. Electrochemical impedance spectroscopy of oxygen reduction reaction (ORR) in a rotating disk electrode configuration: effect of ionomer content and carbon-support. *J Electrochem Soc*. 2015;162(6):F489-F498. doi:10.1149/2.0141506jes
59. Oguz Koroglu E, Civelek Yoruklu H, Demir A, Ozkaya B. In: Mohan SV, Varjani S, Pandey A, eds. *Microbial Electrochemical Technology*. Elsevier; 2019:565.
60. Hjorth Larsen A, Jørgen Mortensen J, Blomqvist J, et al. The atomic simulation environment-a Python library for working with atoms. *J Phys Condens Matter*. 2017;29(27):273002.
61. Giannozzi P, Baroni S, Bonini N, et al. QUANTUM ESPRESSO: a modular and open-source software project for quantum simulations of materials. *J Phys Condens Matter*. 2009;21(39):395502. doi:10.1088/0953-8984/21/39/395502
62. Siahrostami S, Verdaguer-Casadevall A, Karamad M, et al. Enabling direct H_2O_2 production through rational electrocatalyst design. *Nat Mater*. 2013;12(12):1137-1143. doi:10.1038/nmat3795

SUPPORTING INFORMATION

Additional supporting information can be found online in the Supporting Information section at the end of this article.

How to cite this article: Koh KH, Bagherzadeh Mostaghimi AH, Chang Q, et al. Elucidation and modulation of active sites in holey graphene electrocatalysts for H_2O_2 production. *EcoMat*. 2023;5(1):e12266. doi:10.1002/eom2.12266